



Simulations of laminar and turbulent flows over periodic hills with immersed boundary method



Po-Hua Chang, Chuan-Chieh Liao, Hsin-Wei Hsu, Shih-Huang Liu, Chao-An Lin *

Department of Power Mechanical Engineering, National Tsing Hua University, Hsinchu 30013, Taiwan

ARTICLE INFO

Article history:

Received 31 December 2012

Received in revised form 14 August 2013

Accepted 28 October 2013

Available online 9 November 2013

Keywords:

Recirculation

Separation

Reattachment

Immersed boundary method

Large eddy simulation

Wall model

Periodic hills

ABSTRACT

Laminar and turbulent flows over periodic hills are investigated with an immersed boundary method to mimic the curved geometry of the hill within the Cartesian framework. Here, turbulence is modeled through large eddy simulation with and without wall models. For laminar flows examined, flow over periodic hill separates earlier and reattaches later with the increase of Reynolds number. For turbulent flow simulations, Reynolds numbers from 2800 to 10595 are investigated. Predictions without wall models, i.e. assuming linear velocity profile at the wall, return better results both in mean and turbulence quantities, especially for the axial velocity at Reynolds number being 2800 and 5600. The good performance may lay in the fact that at these lower Reynolds numbers, the adopted grid resolves partly the near wall region. Predictions with wall models show a faster recovery of the recirculation zone and excessive diffusive transport across the shear layer. Among the wall models, turbulent boundary layer equation performs marginally better.

© 2013 Elsevier Ltd. All rights reserved.

1. Introduction

Domains with complex rigid boundaries, such as in fluid–solid interaction problems are commonly modeled with body-fitted or unstructured-grid methods. However, the computational cost on grid generation and memory requirements of these methods are generally high when compared with non-boundary conforming methods. Also, modeling complex time-evolving moving-boundary flows requiring transient re-meshing strategies further increases the computational overhead and algorithmic complexity of these approaches. Thus, one would seek to adopt the Cartesian grid based non-boundary conforming methods to address complex fluid–structure interaction problems.

An alternative that not only retains the advantage of structured Cartesian grids but also provides the ability to handle complex geometries is the so-called immersed-boundary method introduced by Peskin [1], where complex geometries within a Cartesian grid can be replaced by generating an external force field that acts on the fluid in the same manner as a solid boundary would. According to Mittal and Iccarino [2], in general, immersed-boundary methods can be roughly categorized as continuous forcing approach and discrete forcing approach. The main problem associated with continuous forcing approaches is the restriction of the time step [3,4]. On the other hand, the discrete forcing approach mainly

for flows with rigid boundary [5,6] explicitly enforces boundary conditions at Eulerian nodes near the immersed boundary. The stability constraint of the time-integration scheme was not degraded [2] compared to its continuous forcing counterpart.

Though the immersed boundary method has been adopted frequently in solving laminar flow problems, however, computing turbulent flows with this method is not as extensive [7,8]. The main difficulty lies in the modeling of the turbulence and the treatment of the near wall region. It is known that commonly adopted eddy viscosity based Reynolds-averaged Navier–Stokes equation (RANS) fails to capture correctly the turbulence anisotropy induced secondary flow [9]. The alternatives are to use explicit algebraic stress model [10,11], non-linear eddy viscosity model [12], Reynolds stress transport model [13,14] or large eddy simulation (LES) [15–19]. Among these models, LES has continued to gain its popularity as a powerful numerical tool to study turbulent flows for engineering applications, where the large eddies of turbulent flows are resolved by a coarser grid and the effect of smaller ones is accounted for by a subgrid-scale model. LES is expected to deliver good turbulent predictions, but the computational demand of wall resolved LES is rather high compared to its RANS counterpart.

To lessen the computational demand of LES, the near wall region is not resolved, and thus the shear stress cannot be determined directly. Instead, wall model is adopted to predict the wall stress. For example, Shumann [20] proposed that the velocity follows the law of the wall and the mean flow quantity has to be known *a priori*. Grozbach [21] and Piomelli et al. [22] further

* Corresponding author. Tel.: +886 3 5742602; fax: +886 3 5722840.

E-mail address: calin@pme.nthu.edu.tw (C.-A. Lin).

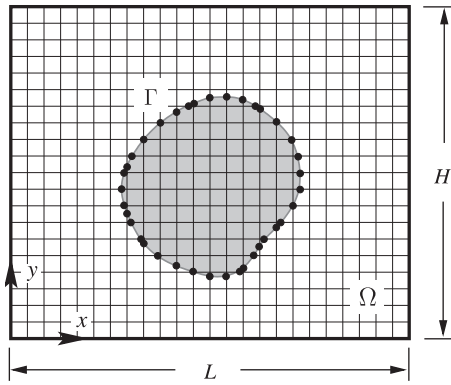


Fig. 1. Flow domain Ω with an immersed boundary Γ .

extended this to use the instantaneous velocity. Instead of adopting the log law distribution, Werner and Wengle [23] on the other hand employed a power law relationship between stress and velocity. To avoid the equilibrium assumption and simple functional relationship, one alternative is using the boundary layer type of equations [24–26] in the near wall region.

In the present study, previously proposed immersed boundary method [6] is used to simulate the laminar and turbulent flows over periodic hills, and turbulence is modeled through large eddy simulation with and without wall models. The flows consist of separation and reattachment of a recirculation zone, which are very sensitive to the treatment of the hill boundary and turbulence modeling. The capability of the present technique is scrutinized by contrasting with available benchmark solution and measurements. The merits of different wall model variants will also be addressed.

2. Methodology

In this section, the general mathematical formulations of the immersed boundary method and turbulence modeling under consideration are first introduced. These are followed by the numerical methods to be employed, and then details of constructing the forcing function needed to represent effects of the immersed boundary. This section is concluded with a fairly detailed description of the complete solution algorithm.

2.1. Mathematical formulation

Consider the problem of a viscous incompressible fluid in a rectangular domain (Ω) containing an immersed massless boundary in the form of a simple closed curve (2D) or surface (3D) Γ , as shown in Fig. 1. It is clear from this figure that few, if any, of the points comprising Γ coincide with grid points.

Table 1
The parallel efficiency for turbulent flows over the periodic hills inside at Reynolds number 10595.

np	Time (s)		
	Momentum	Pressure	Total
Grid arrangements: $200 \times 95 \times 96$			
2	30.7	0.7	33.7
4	16.4	0.7	18.4
8	9.9	0.7	11.3
16	5.8	0.6	6.8
24	3.7	0.6	4.6
32	2.9	0.7	3.8
48	2.2	0.6	3.0

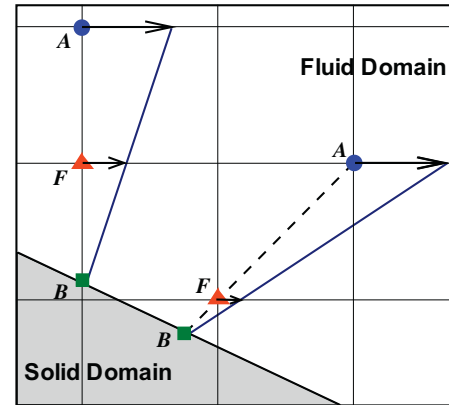


Fig. 2. IBM (1): Location of nodes A, B and forcing point F.

As mentioned above, the influence of the immersed boundary on the fluid is represented by forces exerted on the fluid to impose the no-slip condition at the immersed boundary. Therefore, the governing equations of this fluid–structure interaction system are the usual incompressible Navier–Stokes equations. Since turbulent flow is considered here, large eddy simulation (LES) technique is adopted to model turbulence. Thus, the grid-filtered, incompressible continuity and Navier–Stokes equations take the following forms:

$$\frac{\partial u_i}{\partial x_i} = 0 \quad (1)$$

$$\frac{\partial \rho u_i}{\partial t} + \frac{\partial (\rho u_i u_j)}{\partial x_j} = -\frac{\partial p}{\partial x_i} + \frac{\partial}{\partial x_j} \left[\mu \left(\frac{\partial u_i}{\partial x_j} + \frac{\partial u_j}{\partial x_i} \right) \right] - \frac{\partial \tau_{ij}}{\partial x_j} + f_i \quad (2)$$

where u_i and p are respectively the grid filtered velocity and pressure. ρ is the fluid density, μ is the dynamic viscosity, and τ_{ij} are the sub-grid stresses that are not resolved by the computational grids and have to be modeled. f_i is the forcing function of the immersed boundary method to be defined later. For laminar flow, τ_{ij} is zero.

In the present study, the dynamic model of Gemano et al. [16] is adopted to model the sub-grid stress (SGS),

$$\tau_{ij} - \frac{\delta_{ij}}{3} \tau_{kk} = -2 \underbrace{\rho C_D \Delta^2 |S|}_{\mu_t} S_{ij} \quad (3)$$

where δ_{ij} is the Kronecker delta, $S_{ij} = (\partial u_i / \partial x_j + \partial u_j / \partial x_i) / 2$, $|S| = (2 S_{kl} S_{kl})^{1/2}$ and, Δ defined as $(\Delta x \Delta y \Delta z)^{1/3}$ is the filter width, where the mesh size is a parameter of the filtering operator. For

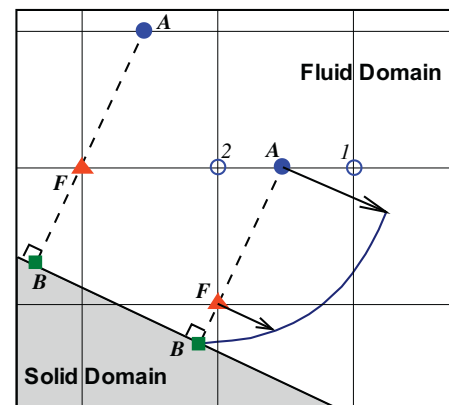


Fig. 3. IBM (2): Location of nodes A, B and forcing point F.

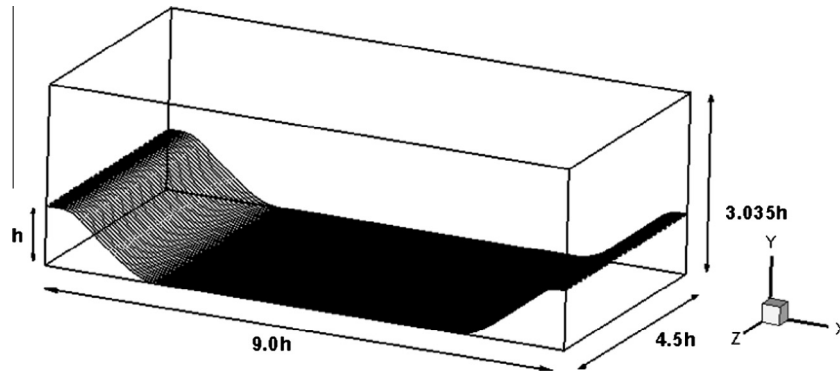


Fig. 4. The geometry of periodic hills.

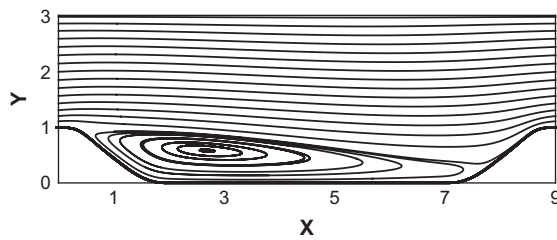


Fig. 5. The structure of recirculation at $Re = 100$.

dynamic model, the model coefficient C_D is allowed to be a function of space and time. Following Lilly [27], the coefficient is obtained using the least square approach.

With the definition of the eddy viscosity, Eq. (2) can be expressed as,

$$\frac{\partial \rho u_i}{\partial t} + \frac{\partial (\rho u_i u_j)}{\partial x_j} = -\frac{\partial p}{\partial x_i} + \frac{\partial}{\partial x_j} \left[\underbrace{(\mu + \mu_t)}_{\mu_{eff}} \left(\frac{\partial u_i}{\partial x_j} + \frac{\partial u_j}{\partial x_i} \right) \right] + f_i \quad (4)$$

where μ_{eff} is effective viscosity comprising both the laminar and eddy viscosities. Laminar flow equation can be recovered by setting μ_t to be zero.

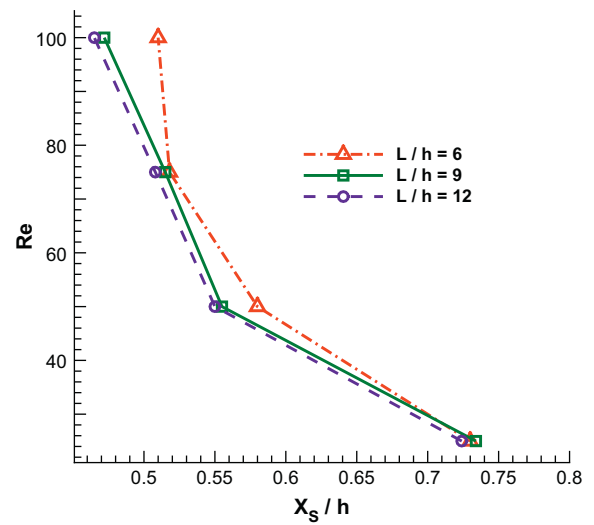


Fig. 7. Variation of separation point with Reynolds number and inter-hill distance.

2.2. Numerical algorithm

The numerical procedure used herein is based on a finite volume method for Eq. (4) in the Cartesian coordinates with a

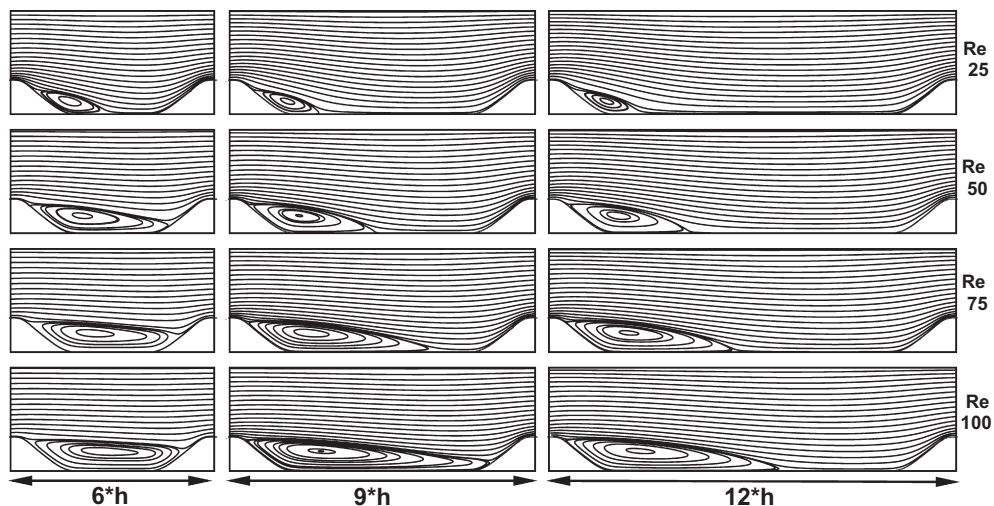


Fig. 6. The streamlines with different inter-hill distances and Reynolds numbers.

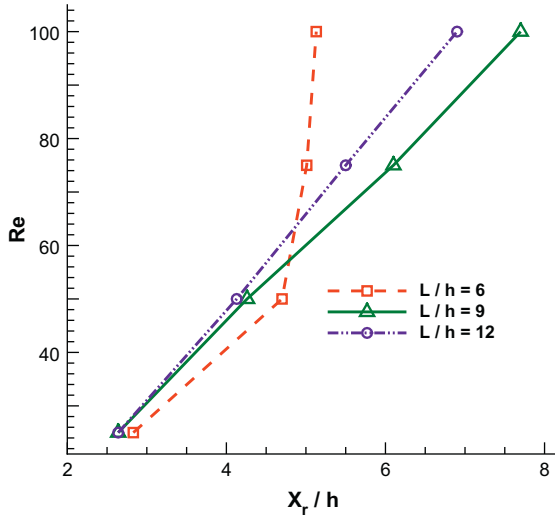


Fig. 8. Variation of reattachment point with Reynolds number and inter-hill distance.

staggered-grid arrangement of dependent variables [6,19]. A fractional-step (projection) method implemented with a combination of the Adams–Bashforth and the Crank–Nicholson methods for the advective and diffusive terms, respectively, is used for the

temporal discretization. Due to its storage economy and straightforward implementation of boundary condition, this time-advancement formulation was employed by Choi and Moin [28] for the sequential flow simulation.

Key steps in the numerical procedure are shown as follows. $(u_i^{(m)}, p^{(m)})$ are assumed to be known at the current time $m\Delta t$, where a uniform time step, Δt , is employed. $(u_i^{(m+1)}, p^{(m+1)})$ at the next time, $(m+1)\Delta t$, are obtained through the following four sub-steps in the semi-discrete form:

$$\begin{aligned} \rho \frac{u_i^* - u_i^{(m)}}{\Delta t} + \rho \frac{\partial}{\partial x_j} \left(\frac{3}{2} u_i^{(m)} u_j^{(m)} - \frac{1}{2} u_i^{(m-1)} u_j^{(m-1)} \right) \\ = - \frac{\partial p^{(m)}}{\partial x_i} + \frac{3}{2} D_{i,xz}^{(m)} - \frac{1}{2} D_{i,xz}^{(m-1)} + \frac{1}{2} (D_{i,y}^* + D_{i,y}^{(m)}) + f_i^{(m+1)} + f_{df}^{(m+1)} \end{aligned} \quad (5)$$

$$\rho \frac{u_i^* - u_i^*}{\Delta t} = \frac{\partial p^{(m)}}{\partial x_i} \quad (6)$$

$$\frac{\partial}{\partial x_i} \frac{\partial p^{(m+1)}}{\partial x_i} = \frac{\rho}{\Delta t} \frac{\partial u_i^*}{\partial x_i} \quad (7)$$

$$\rho \frac{u_i^{(m+1)} - u_i^*}{\Delta t} = - \frac{\partial p^{(m+1)}}{\partial x_i} \quad (8)$$

where f_{df} is the driving force to be defined latter. $D_{i,xz}$ and $D_{i,y}$ are diffusion terms and x , z and y stand for the stream-wise, the

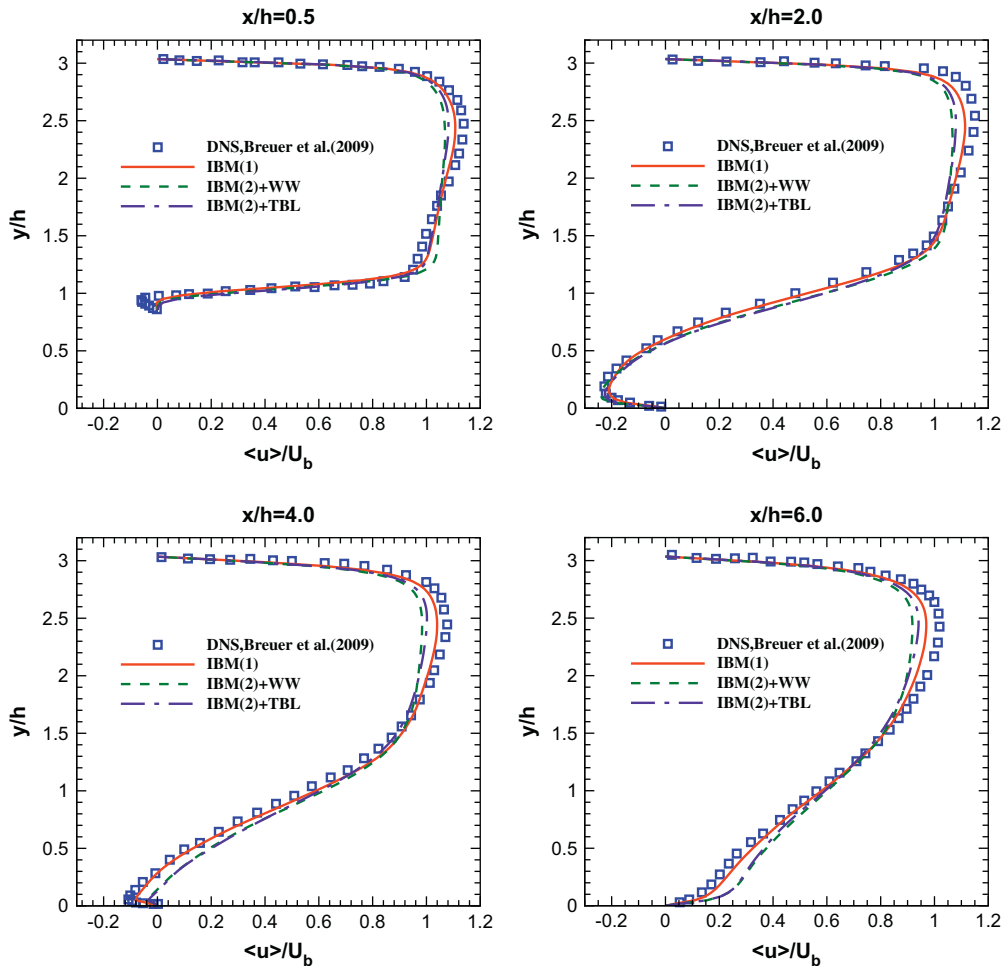


Fig. 9. Mean velocity $\langle u \rangle$ at $Re = 2800$.

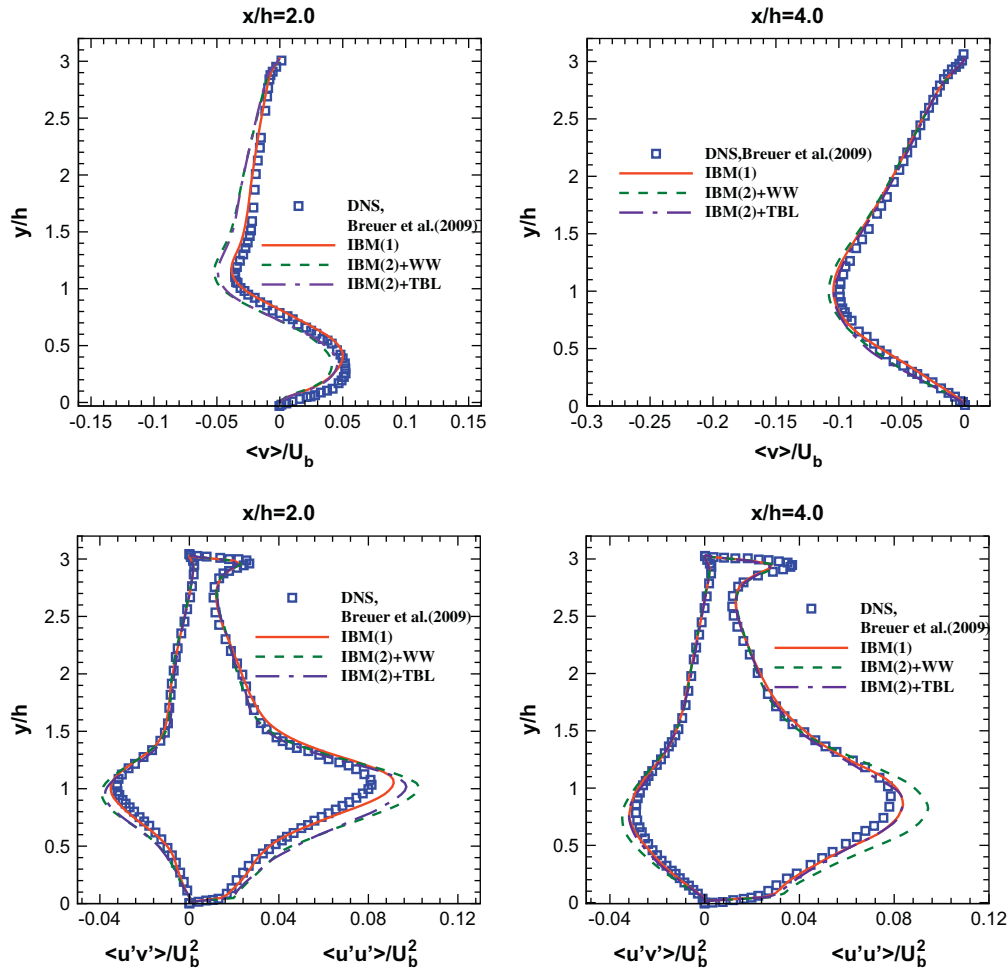


Fig. 10. Normal stress $\langle u'u' \rangle$ and shear stress $\langle u'v' \rangle$.

span-wise, and the transverse directions, respectively. For example, $D_{i,y}^{(*)}$ is defined as,

$$D_{i,y}^{(*)} = \frac{\partial}{\partial x_y} \left[(\mu + \mu_t^{(m)}) \left(\frac{\partial u_i^{(*)}}{\partial x_y} + \frac{\partial u_y^{(*)}}{\partial x_i} \right) \right]$$

All spatial derivatives are approximated by using second-order centered difference scheme. Since the Crank–Nicholson scheme is applied in the y direction in Eq. (5), the discretized algebraic equations from momentum equations are solved by the TriDiagonal Matrix Algorithm (TDMA) solver. In each time step a Poisson equation is solved to obtain a divergence free velocity field. Because the grid spacing is uniform in the streamwise and spanwise direction, together with the adoption of the periodic boundary conditions, Fourier transform can be used to reduce the 3-D Poisson equation to uncoupled 1-D algebraic equations. The algebraic equations are solved by the TDMA solver. Alternatively, without adopting Fourier transform, the most time consuming 3D pressure Poisson equation can be solved by the CGSTAB method of Van Den Vorst and Sonneveld [29]. The former approach is adopted here.

In the present parallel implementation, the single program multiple data (SPMD) environment is employed. Message-Passing Interface (MPI) is adopted for communication between the processors. The domain decomposition is done on the spanwise direction of the computational domain, where ghost cells are adopted along the inter-processor boundary [30]. However, since the domain decomposition is performed in the span-wise direction, thus all to all communication due to the Fourier transform becomes the

bottle neck of the parallel performance. Table 1 shows the computational time for the 10595 Reynolds number case using IBM-1350 cluster. Regardless of the number processor used, the time used for the 1-D Poisson equation is fixed, which is mainly used for the inter-processor communications for Fourier transform. Thus, this method is more suitable for lower number of processors [31].

To evaluate Eq. (5), the forcing $f_i^{(m+1)}$ must be determined in advance to satisfy the no-slip boundary condition on any immersed boundary at the advanced time level. This will be treated in the next subsection.

2.3. Forcing strategies

The force applied to the computational node due to presence of a solid body must be determined at the advanced time level before the solution procedure presented in Eqs. (5)–(8) can be started. This force (per unit mass) is simply a Newtonian acceleration of any node near the solid body.

Thus,

$$f_i^{(m+1)} = \frac{u_{i,F} - \hat{u}_i}{\Delta t} \quad (9)$$

where \hat{u}_i is an estimate of the time-level $(m+1)$ velocity field in a neighborhood of the solid boundary in the absence of forcing, and $u_{i,F}$ is the velocity (at the same location) when forcing is taken into account. Here, \hat{u}_i is estimated with a simple, explicit Adams–Bashforth scheme where Eq. (4) is provisionally discretized explicitly in

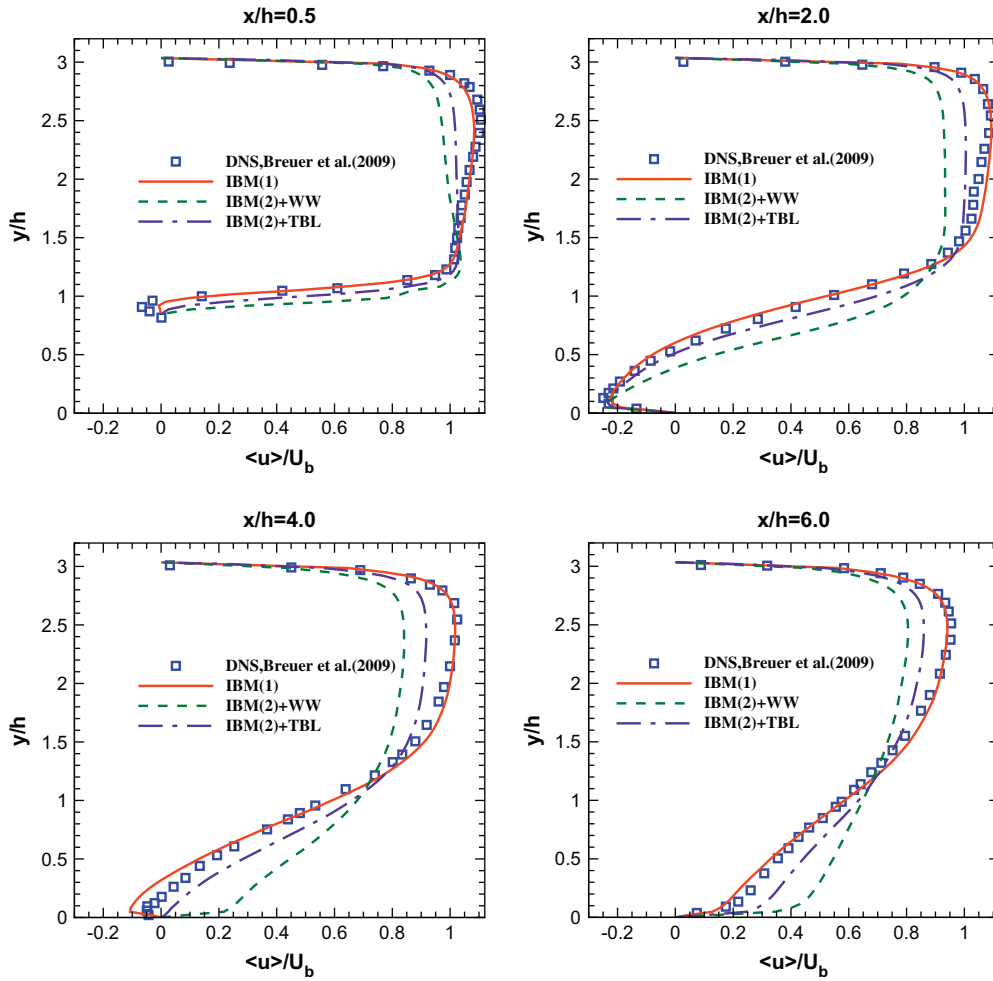


Fig. 11. Mean velocity $\langle u \rangle$ at $Re = 5600$.

time to derive the momentum forcing value, as described in Kim et al. [32]:

$$\hat{u}_i = u_i^{(m)} - \Delta t \left\{ \frac{3}{2} \left[\frac{\partial(u_i u_j)}{\partial x_j} - D_i \right]^{(m)} - \frac{1}{2} \left[\frac{\partial(u_i u_j)}{\partial x_j} - D_i \right]^{(m-1)} + \frac{\partial p^{(m)}}{\partial x_i} \right\} \quad (10)$$

The issue of computing the forcing function f_i of Eq. (9), and hence $u_{i,F}$, when the interface does not coincide with grid nodes is discussed here.

The forcing strategy adopted here consists of two parts, i.e. interpolation (at forcing points in the fluid domain) and a solid-body-forcing procedure, the latter of which leads to improved accuracy (in particular, significant reduction of non-physical temporal oscillations of dependent variables) when treating moving boundaries [6]. Thus, two issues should be addressed here, i.e. the forcing location in the fluid region, and the solid-body forcing.

A schematic of forcing points in the fluid region used to calculate $u_{i,F}$ is shown in Fig. 2. This is carried out via a linear interpolation technique in [6] and is adopted in the present study, which is termed IBM (1). From the figure it can be seen that forcing nodes are Cartesian grid points outside the solid body, but immediately adjacent to it. The no-slip condition is imposed at points of the boundary, Γ , of the solid body at points \mathbf{x}_B lying on the same grid line as the forcing point \mathbf{x}_F . Then the velocity $u_{i,F}$ at this point is obtained by (linear) interpolation between points \mathbf{x}_B and \mathbf{x}_A , with

the latter being the next point outward from \mathbf{x}_F on the grid line containing points \mathbf{x}_B and \mathbf{x}_F . Thus, for the u velocity component at the point $u_{i,F}$ in the inset to Fig. 2,

$$u_{i,F} = \hat{u}_A - \left(\frac{\hat{u}_A - \hat{u}_B}{\mathbf{x}_A - \mathbf{x}_B} \right) (\mathbf{x}_A - \mathbf{x}_F) \quad (11)$$

with analogous computations used, scalarly, for other velocity components.

This leads to direct calculation of $f_i^{(m+1)}$ via substitution of (10) and (11) into Eq. (9):

$$f_i^{(m+1)} = \frac{u_{i,F} - u_i^{(m)}}{\Delta t} + \frac{3}{2} \left[\frac{\partial(u_i u_j)}{\partial x_j} - D_i \right]^{(m)} - \frac{1}{2} \left[\frac{\partial(u_i u_j)}{\partial x_j} - D_i \right]^{(m-1)} + \frac{\partial p^{(m)}}{\partial x_i} \quad (12)$$

The linear interpolation procedure to compute $u_{i,F}$ in Eq. (11) is valid for laminar flow or turbulent flow for velocity in the viscous sublayer. For velocity outside the viscous sublayer, the velocity may not vary linearly towards the wall. Thus other measures have to be taken. The present approach is similar to the wall function approach along the flat wall. Therefore, $u_{i,F}$ is now predicted by wall models, as shown in Fig. 3 (IBM (2)). Also, line $\overline{x_B x_A^*}$ is now perpendicular to the immersed boundary. Here, $\hat{u}_{i,A}$ is obtained through linear interpolation from the known values, and the goal is to find $u_{i,F}$, and hence the forcing value.

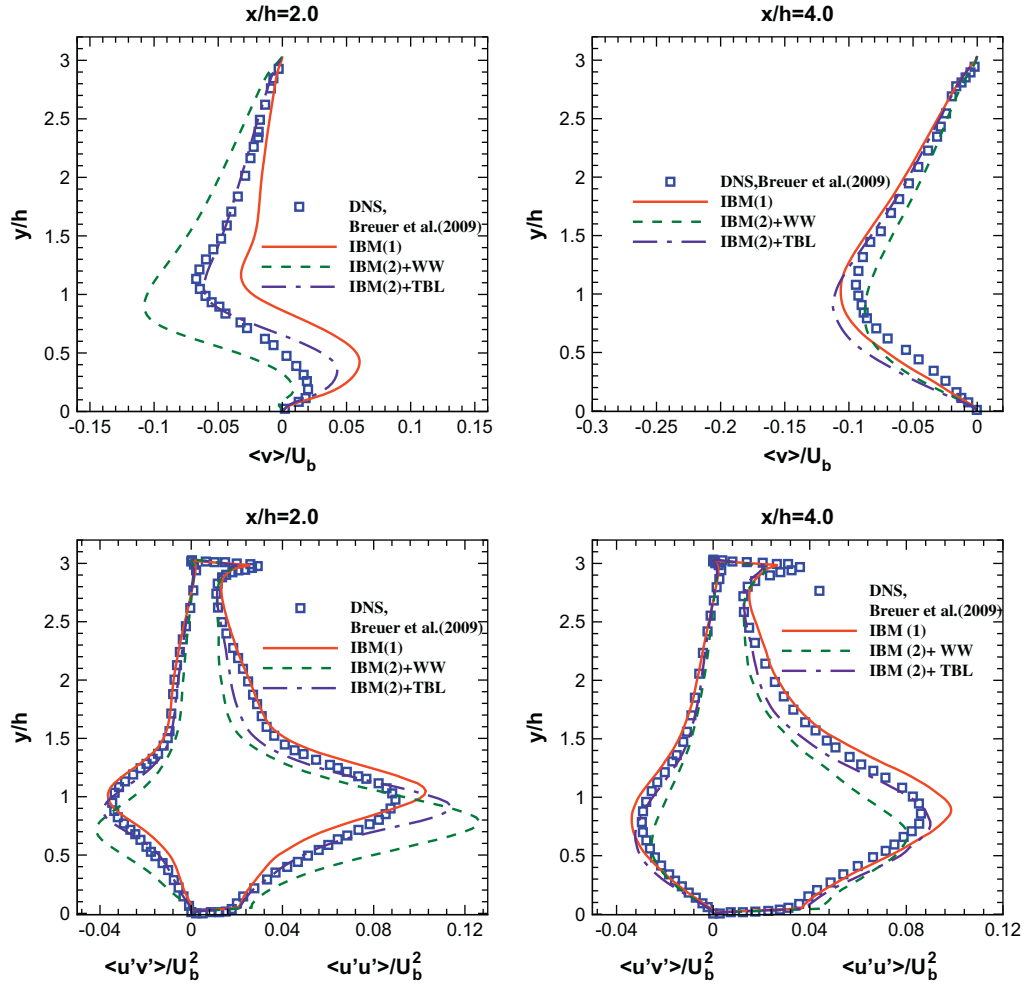


Fig. 12. Normal stress $\langle u'u' \rangle$ and shear stress $\langle u'v' \rangle$ at $Re = 5600$.

Here, two types of wall models are adopted, i.e. Werner-Wengle model (WW) [23] and the turbulent boundary layer equation (TBL) [26]. The Werner and Wengle model was reported in [33] to perform best among several wall models. Werner and Wengle [23] proposed that the law of the wall is a $1/7$ power law outside the viscous sublayer and linear profile otherwise, i.e.

$$u^+ = \begin{cases} y^+, & \text{if } y^+ \leq 11.8 \\ 8.3(y^+)^{1/7}, & \text{if } y^+ > 11.8 \end{cases} \quad (13)$$

where $u^+ = u/u_\tau$ and $y^+ = u_\tau y_n/v_\tau$ is the local friction velocity and y_n is the normal distance from the wall. Since the velocity $u_i(\mathbf{x}_A)$ and distance from the wall $y_n(\mathbf{x}_A)$ at node \mathbf{x}_A are known, then using Eq. (13), the friction velocity can be obtained and hence $u_{i,F}$.

The other wall model adopted is assuming that the turbulent boundary layer equation (TBL) [26] holds at the near wall region by neglecting the normal wall velocity, i.e.

$$\frac{\partial}{\partial n}(v + v_t) \frac{\partial u_i}{\partial n} = F_i \quad (14)$$

and

$$F_i = \frac{1}{\rho} \frac{\partial p}{\partial x_i} + \frac{\partial u_i}{\partial t} + \frac{\partial u_i u_j}{\partial x_j} \quad (15)$$

where n and i represent the wall normal and parallel directions, respectively. The eddy viscosity v_t in Eq. (14) is damped towards the wall using van Driest damping function, i.e.

$$\frac{v_t}{v} = ky^+(1 - e^{-y^+/A})^2 \quad (16)$$

where $k = 0.4$ is the von Karman's constant, and $A = 19$.

The wall shear stress is obtained by integrating Eqs. (14) and (15) from wall node (\mathbf{x}_B) to the next point outward from the forcing node, i.e. (\mathbf{x}_A). Thus, the wall stress is expressed as [26],

$$\tau_{wi} = \mu \left. \frac{\partial u_i}{\partial n} \right|_w = \frac{\rho}{\int_0^{y_n(\mathbf{x}_A)} \frac{dy}{v + v_t}} \left(u_i(\mathbf{x}_A) - F_i \int_0^{y_n(\mathbf{x}_A)} \frac{y dy}{v + v_t} \right) \quad (17)$$

where τ_{wi} is the wall stress and $y_n(\mathbf{x}_A)$ is the distance from node \mathbf{x}_A to the wall. For simplicity, the equilibrium stress model [26] is adopted here, i.e. $F_i = 0$.

It should be noted that previous studies [23,26] imposed the obtained shear stress at the wall. However, in the present study, the obtained velocity, i.e. $u_{i,F}$, is imposed at the first off wall node through forcing, as shown in Fig. 3.

2.4. Geometry and boundary conditions

The considered geometry with periodic polynomial-shaped obstacles experimented by Almeida et al. [34] is shown in Fig. 4, where the height of the hill and the length of the periodic hills are respectively at h and $9h$ and the height of the channel is $3.035h$. For LES simulation, the spanwise dimension is $4.5h$, whereas for laminar flow simulation, this dimension is h . The

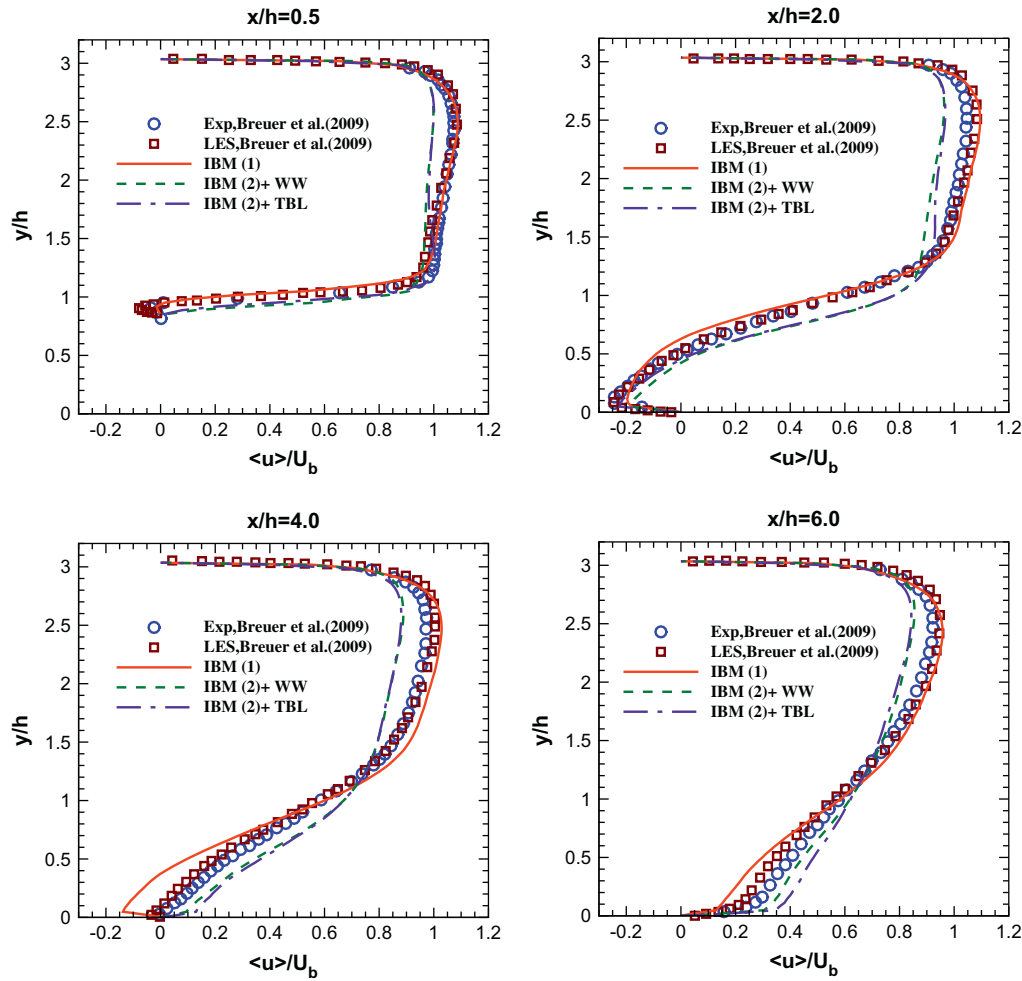


Fig. 13. Mean velocity $\langle u \rangle$ at $Re = 10595$.

definition of the Reynolds number is based on the bulk velocity (U_B) above the crest of the hill, i.e. $Re = \frac{U_B h}{\nu}$.

In the present study, the flow field is driven by a driving force determined by the prescribed bulk Reynolds number [19]. To maintain the bulk Reynolds number, the driving force is modified at each time step based on the difference of U_B and the predicted bulk velocity U_{av} , i.e.,

$$f_{df}^{(m+1)} = f_{df}^{(m)} + \rho \left(\frac{U_B - U_{av}^{(m)}}{\Delta t} \right)$$

For laminar and turbulent flows, no slip and wall laws boundary condition are respectively applied along the top and bottom, and along the immersed boundary along the hills. Periodic boundary is employed in both the streamwise and spanwise directions. For all the computations, grid is uniformly spaced in the streamwise and spanwise directions, while in the transverse direction the grid is non-uniform.

3. Numerical results

3.1. Laminar flows over periodic hills

Attention is directed first to the laminar flow over periodic hills. The adopted Reynolds numbers are in the range of $25 \leq Re \leq 100$, which are laminar and two-dimensional in nature [8]. For this laminar flow simulation, the computation of the forcing node along the

immersed boundary is as previously shown in Fig. 2, i.e. IBM (1). Grid of size $(250 \times 182 \times 16)$ is adopted, which was tested to be adequate for this range of flows.

Streamlines can be used to examine the flow patterns. The streamline is obtained by solving the stream function equation, i.e.

$$\frac{\partial^2 \Psi}{\partial x^2} + \frac{\partial^2 \Psi}{\partial y^2} = \frac{\partial u}{\partial y} - \frac{\partial v}{\partial x} \quad (18)$$

Fig. 5 shows the predicted streamlines at Reynolds number being 100, where the recirculating structure can be clearly observed. To validate the present predictions, the locations of the separating and reattaching points are contrasted with the results in Breuer et al. [8]. The present separation point locates at $x_s/h = 0.472$ and reattachment point at $x_r/h = 7.7$, which are in good agreement with those in [8], respectively at $x_s/h = 0.45$ and $x_r/h = 7.73$.

Focus is next directed to investigate the influences of the inter-hill distances and Reynolds numbers on the vortex structure and the separating and reattaching lengths. The lengths of the channel are chosen to be $6h$, $9h$ and $12h$, and Reynolds numbers are 25, 50, 75 and 100. Fig. 6 presents the streamlines with different inter-hill distances under different Reynolds numbers. It can be clearly observed that the size of the recirculation zone increases in tandem with the increase of the Reynolds number, except in the $6h$ inter-hill distance, where the vortex is hindered by the downstream hill. Quantitative observation of the separating and reattaching locations can be referred to Figs. 7 and 8. Clearly, the influence of the

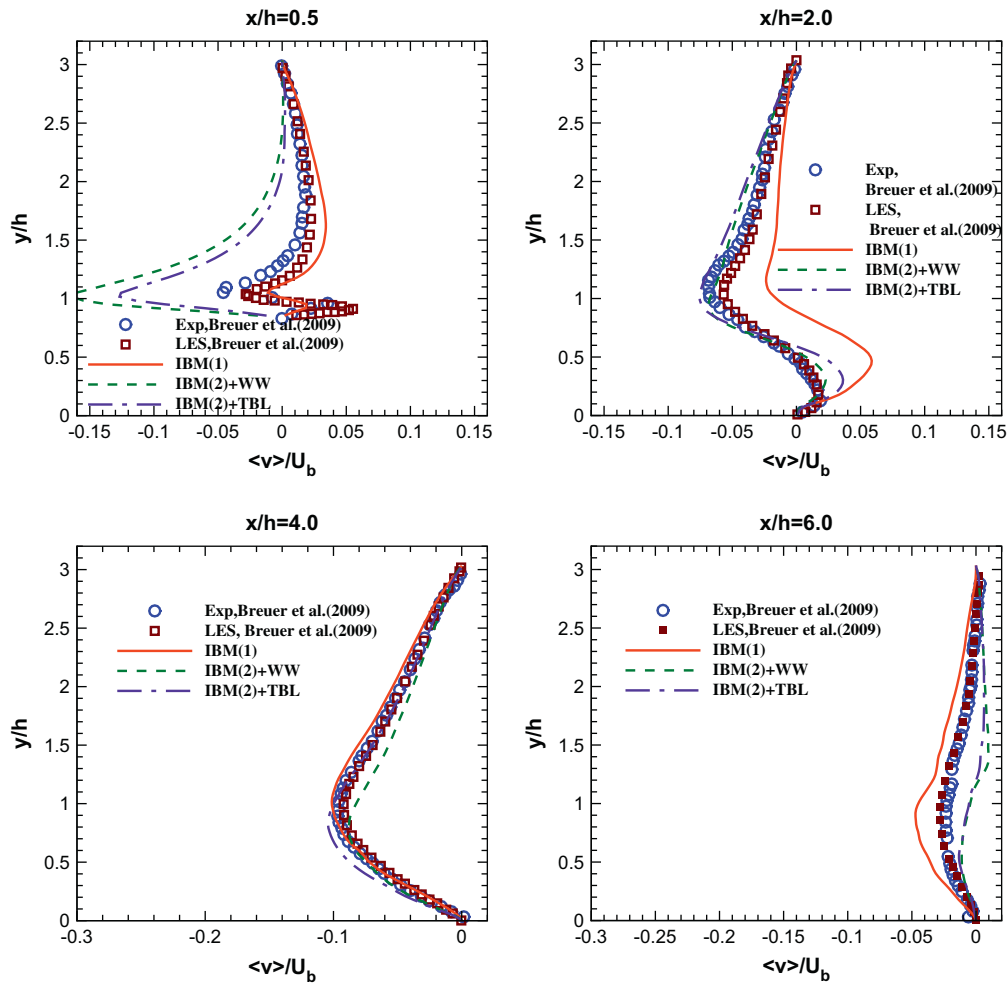


Fig. 14. Mean velocity $\langle v \rangle$ at $Re = 10595$.

inter-hill distance is not as significant as the Reynolds number. For the range of Reynolds number investigated, flow over periodic hill separates earlier and reattaches later with the increase of Reynolds number. Also, reattaching length scales linearly with the Reynolds number for inter-hill distance greater than $9h$.

3.2. Turbulent flows over periodic hills

Here, turbulent periodic hill flows at $Re = 2800$, 5600 , and 10595 are simulated with LES using immersed boundary method. Since the wall region is not resolved in the present simulation, wall models are used here, i.e. Werner-Wengle model (WW) [23] and the turbulent boundary layer equation (TBL) [26]. The adoption of the wall model necessitates the computations of the parallel wall components. Thus, the arrangement of the forcing nodes and velocity along the immersed boundary is shown in Fig. 3. Simulation is also performed using IBM (1) (Fig. 2) without wall modeling. Grid of size $(200 \times 95 \times 96)$ is adopted, where $\Delta x_{crest}/h = 0.045$, $\Delta y_{crest}/h = 0.032$ and $\Delta z_{crest}/h = 0.047$ at the hill crest are compatible to those used in the resolved LES of Temmerman et al. [33], which is based on the curvilinear grid with wall model. The present predictions are contrasted with the resolved LES and DNS data, and measurements of Breuer et al. [8].

The predicted mean and Reynolds stresses for $Re = 2800$ are shown in Fig. 9 and 10. At this Reynolds number, without wall model, predictions of IBM (1) return the best results both in mean and turbulence quantities compared with the DNS data of Breuer

et al. [8]. Predictions with wall models show a slightly faster recovery of the recirculation zone beyond $x/h = 4$, which is due to the higher level of shear stresses predicted further upstream, for example at $x/h = 2$. The good performance of IBM (1) may lay in the fact that at this low Reynolds number the adopted grid resolves partly the near wall region. Among the wall models, TBL performs marginally better.

At higher Reynolds number, i.e. $Re = 5600$, IBM (1) still outperforms the wall models as shown in Fig. 11 for the streamwise velocity. At $x/h = 0.5$, the shear layer is not correctly predicted by the wall models, whereas IBM (1) predicts the small reverse flow correctly. Also, the wall models predict too high levels of flow recovery and hence a rapid deceleration of the core flow at $y/h = 2$. Among the wall models, again TBL is better, though the diffusive transport is still excessive. Fig. 12 shows that shear stress is better predicted by IBM (1) and TBL, and this confirms the development of the streamwise velocity.

Fig. 13 shows the predicted streamwise velocity at $Re = 10595$ where both the measurements and resolved LES data [8] are available for comparisons. At $x/h \leq 2$, IBM (1) performs best, especially the small reverse flow at $x/h = 0.5$. At $x/h \geq 4$, IBM (1) still outperforms the wall models, though it predicts a slight slower recovery of the near wall velocity. On the other hand, the higher diffusive nature of the wall models is still evident in this Reynolds number. The mean vertical velocity and turbulence quantities are shown in Figs. 14 and 15. For the shear stress, IBM (1)'s predictions are compatible with the resolved LES in [8], except at $x/h = 2$ where

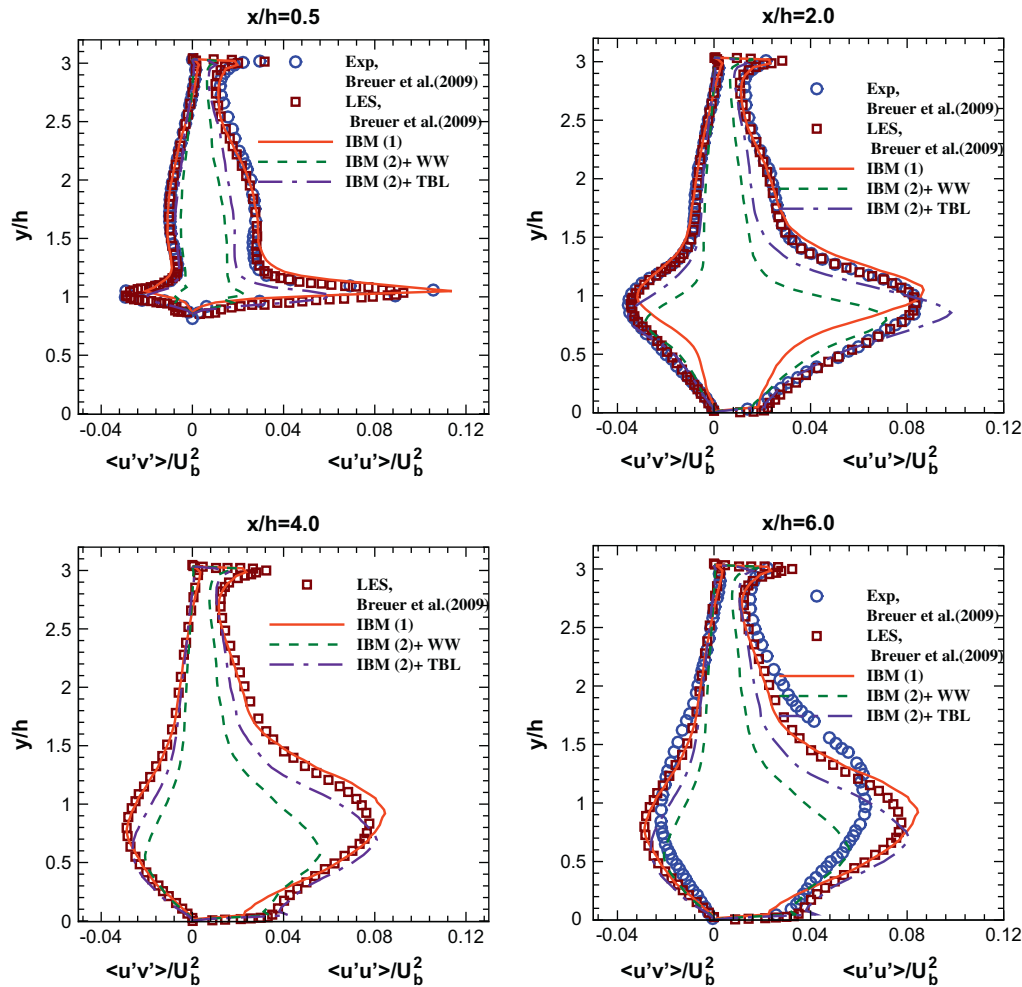


Fig. 15. Normal stress $\langle u'u' \rangle$ and shear stress $\langle u'v' \rangle$ at $Re = 10595$.

a lower level is predicted near the bottom wall. Among the wall models, TBL performs relatively better.

4. Conclusion

Laminar and turbulent flows over the periodic hills are investigated. An immersed boundary method is used to mimic the *curvilinear* geometry of the hill, and turbulence is modeled through large eddy simulation with and without wall models. Laminar flows at Reynolds numbers 25 to 100 are investigated first. For the range of Reynolds number examined, flow over periodic hill separates earlier and reattaches later with the increase of Reynolds number. Also, reattaching length scales linearly with the Reynolds number. For turbulent flow simulations, forcing is applied to the velocity at first wall-off node, which is obtained by the wall models or linear interpolation. This is contrast to previous wall model implementation, where instead the wall stress is imposed. Reynolds numbers from 2800 to 10595 are investigated. Predictions without wall models, i.e. IBM (1) (assuming linear profile at the wall), return better results both in mean and turbulence quantities, especially for the axial velocity at Reynolds number being 2800 and 5600. Predictions with wall models show a faster recovery of the recirculation zone. Among the wall models, TBL performs marginally better. The good performance of IBM (1) may lay in the fact that at lower Reynolds number, the adopted grid resolves partly the near wall region.

Acknowledgments

The research work is supported by the National Science Council of Taiwan, Low carbon research center of NTHU and the computational facilities are provided by the National Center for High-Performance Computing of Taiwan which the authors gratefully acknowledge.

References

- [1] Peskin CS. Flow patterns around heart valves: a numerical method. *J Comput Phys* 1972;10:252–71.
- [2] Mittal R, Iaccarino G. Immersed boundary methods. *Annu Rev Fluid Mech* 2005;37:239–61.
- [3] Saiki EM, Biringen S. Numerical simulation of a cylinder in uniform flow: application of a virtual boundary method. *J Comput Phys* 1996;123:450–65.
- [4] Lai MC, Peskin CS. An immersed boundary method with formal second-order accuracy and reduced numerical viscosity. *J Comput Phys* 2000;160:705–19.
- [5] Mohd Yusof J. Combined immersed boundary/B-spline methods for simulations of flow in complex geometries. Center of Turbulence Research Annual Research Briefs; 1997.
- [6] Liao CC, Chang YW, Lin CA, McDonough JM. Simulating flows with moving rigid boundary using immersed-boundary method. *Comput Fluids* 2010;39:152–67.
- [7] Balaras E. Modeling complex boundaries using an external force field on fixed Cartesian grids in large-eddy simulations. *Comput Fluids* 2004;33:375–404.
- [8] Breuer M, Peller N, Rapp Ch, Manhart M. Flow over periodic hills-numerical and experimental study in a wide range of Reynolds number. *Comput Fluids* 2009;38:433–57.
- [9] Demuren AO, Rodi W. Calculation of turbulence-driven secondary motion in non-circular ducts. *J Fluid Mech* 1984;140:189–222.
- [10] Spiezale CG. On nonlinear k-l and k-ε models of turbulence. *J Fluid Mech* 1987;178:495–475.

- [11] Chiu TH, Yeh LK, Lin CA. Explicit algebraic stress modelling of homogeneous and inhomogeneous flows. *Int J Numer Methods Fluids* 2005;49:817–35.
- [12] Craft TJ, Launder BE, Suga K. Development and application of a cubic eddy-viscosity model of turbulence. *Int J Heat Fluid Flow* 1996;17:108–15.
- [13] Launder BE, Li SP. On the elimination of wall-topography parameters from second moment closure. *Phys Fluids* 1994;6:999–1006.
- [14] Tsao JM, Lin CA. Reynolds stress modelling of jet and swirl interaction inside a gas turbine combustor. *Int J Numer Methods Fluids* 1999;29:451–64.
- [15] Smagorinsky J. General circulation experiments with the primitive equations. *Mon Weather Rev* 1963;91:99–164.
- [16] Germano M, Piomelli U, Moin P, Cabot W. A dynamic subgrid-scale eddy viscosity model. *Phys Fluids A* 1991;3:1760–5.
- [17] Madabhushi RK, Vanka SP. Large eddy simulation of turbulence driven secondary flow in a square duct. *Phys Fluids A* 1991;3:2734–45.
- [18] Lo W, Lin CA. Mean and turbulence structures of Couette–Poiseuille flows at different mean shear rates in a square duct. *Phys Fluids* 2006;18:068103.
- [19] Hsu HW, Hsu JB, Lo W, Lin CA. Large eddy simulations of turbulent Couette–Poiseuille and Couette flows inside a square duct. *J Fluid Mech* 2012;702:89–101.
- [20] Schumann U. Subgrid-scale model for finite difference simulation of turbulent flows in plane channels and annuli. *J Comput Phys* 1975;18:376–404.
- [21] Grotzbach G. Direct numerical and large eddy simulation of turbulent channel flows. In: Cheremisinoff NP, editor. *Encyclopedia of fluid mechanics*; 1987. p. 1337–91.
- [22] Piomelli U, Ferziger J, Moin P, Kim J. New approximate boundary conditions for large eddy simulations of wall-bounded flows. *Phys Fluids A* 1989;1:1061–989.
- [23] Werner H, Wengle H. Large-eddy simulation of turbulent flow over and around a cube in a plate channel. In: *8th Symposium on turbulent shear flows*; 1991. p. 155–68.
- [24] Balaras E, Benocci C, Piomelli U. Two-layer approximate boundary conditions for large-eddy simulations. *AIAA J* 1996;34:1111–9.
- [25] Cabot W, Moin P. Approximate wall boundary conditions in the large-eddy simulation of high Reynolds number flow. *Flow Turbul Combust* 1999;63:269–91.
- [26] Wang M, Moin P. Dynamic wall modeling for large-eddy simulation of complex turbulent flows. *Phys Fluids* 2002;14:2043–51.
- [27] Lilly DK. A proposed modification of the Germano subgrid-scale closure method. *Phys Fluids* 1992;4:633–5.
- [28] Choi H, Moin P. Effects of the computational time step on numerical solutions of turbulent flow. *J Comput Phys* 1994;113:1–4.
- [29] Van den Vorst HA, Sonneveld P. CGSTAB, a more smoothly converging variant of CGS. Technical Report 90-50, Delft University of Technology; 1990.
- [30] Hsu HW, Hwang FN, Wei ZH, Lai SH, Lin CA. A parallel multilevel preconditioned iterative pressure Poisson solver for the large-eddy simulation of turbulent flow inside a duct. *Comput Fluids* 2011;45:138–46.
- [31] Gorobets A, Trias FX, Soria M, Oliva A. A scalable parallel Poisson solver for three-dimensional problems with one periodic direction. *Comput Fluids* 2010;39:525–38.
- [32] Kim J, Kim D, Choi H. An immersed-boundary finite-volume method for simulations of flow in complex geometries. *J Comput Phys* 2001;171:132–50.
- [33] Temmerman L, Leschziner MA, Mellen CP, Fröhlich J. Investigation of wall-function approximations and subgrid-scale models in large eddy simulation of separated flow in a channel with streamwise periodic constrictions. *Int J Heat Fluid Flow* 2003;24:157–80.
- [34] Almeida GP, Durao DFG, Heitor MV. Wake flows behind two-dimensional model hills. *Exp Therm Fluid Sci* 1993;7:87–101.